Advanced Steel Construction – Vol. 21 No. 3 (2025) 231–242
DOI:10.18057/IJASC.2025.21.3.5

A PROPOSAL OF SIMPLIFIED SEISMIC DESIGN METHOD FOR STEEL PIER WITH POTENTIAL FAILURE MODES OF LOCAL INSTABILITY AND ULTRA-LOW CYCLE FATIGUE

Cheng Cheng, Xu Xie * and Tian-Jia Wang

College of Civil Engineering and Architecture, Zhejiang University, Hangzhou, China
** (Corresponding author: E-mail: xiexu@zju.edu.cn)*

ABSTRACT

Local instability (LI) and ultralow-cycle fatigue (ULCF) are two potential failure modes of steel piers subjected to strong earthquakes. Steel bridges constructed in highly seismic regions must account for both failure modes in their seismic design calculations. While the issue of LI has largely been addressed, with preventive measures incorporated into various bridge design codes, the ULCF assessment remains challenging due to its high computational cost. Therefore, investigating the conditions under which the ULCF assessment can be avoided is of great significance for simplifying the seismic design of steel bridges. To this end, this study focuses on the damage occurrence priority of the two failure modes of steel piers. The proposed simplified seismic design method is the avoidance of ULCF check by constructing piers with the failure occurrence priority of LI. Taking the widely used box section single-column steel pier as an example, 90 piers with different structural parameters, representative of practical engineering applications, were designed in this paper. Based on a hypothetical cyclic loading protocol, the parameter ranges of steel piers with different damage priorities were determined. Discussion on the seismic performance of piers showed that the order of failure occurrence sequence is controlled by the mechanical properties of pier structure, rather than the load conditions it is subjected to. Additionally, the credibility of the derived damage occurrence sequence and the simplified seismic design method was verified through dynamic analyses using real seismic wave inputs. The work shown in this paper can serve as a reference to simplify the seismic design process of steel piers.

ARTICLE HISTORY

Received: 20 April 2024
Revised: 7 January 2025
Accepted: 8 January 2025

KEYWORDS

Local instability;
Ultralow-cycle fatigue;
Damage occurrence priority;
Seismic design;
Steel pier

1. Introduction

The local instability (LI) and the ultralow-cycle fatigue (ULCF) are two typical failure modes of steel piers exposed to strong earthquakes. The LI damage is characterized as the bending of steel plates accumulated in a local area of flange or web, which eventually results in the significant deterioration of the bearing capacity. While, the ULCF damage starts from the premature cracks aroused by several cycles of extremely large strain loops, followed by the stable growth of cracks and the sudden crack propagation under subsequent cyclic loads. The ULCF life of steel structures is within the range of very few cycles, that is, usually less than 20 loading cycles [1-2]. The plasticity of steel cannot be fully utilized until the final failure. Severe damage, including these two failure modes, was widely observed during the Northridge earthquake in 1994 and the Kobe earthquake in 1995 [3-5]. Since then, extensive experimental and analytical investigations on the seismic performance of steel piers have been conducted [4-12]. Up to now, researchers have reached the consensus of the coexistence of LI and ULCF and the fatality of the two failure modes.

During the past 30 years, scholars have conducted various studies on the LI failure of steel piers. For example, based on experimental findings, Ge et al. defined the point at which the bearing capacity of steel piers reaches its maximum value and subsequently decreases to 95% as the limit state to determine the initiation of LI damage in pier structures [13]. Goto et al. proposed a limit state criterion for steel piers from an energy prospect by testing pier specimens under different loading histories [14]. Based on the numerical investigation, Gao et al. established several empirical formulae of the limit state values for providing guidance of seismic design of steel piers [15]. At present, the LI failure of steel piers has been basically solved, and the relevant provisions can be found in bridge design codes of various countries [16-18].

Great efforts have been devoted to developing effective ULCF assessment methods, which can be divided into two categories according to their analytical dimension. One category involves the empirical methods modified from the Coffin-Manson law [19-20] applied in the low-cycle fatigue field (LCF). Examples of these methods include the Tateishi model [21], the Xue model [22], and the macro deformation history-based assessment method [23]. However, Tamura et al. have demonstrated that the triaxial stress states within the damage area has significant influence on the material ductility from the tensile-shear tests of structural steels [24-25], which is contrary to the practice of using plastic strain as the only calculation factor adopted in the empirical methods. Direct application of the empirical methods in engineering structures lacks sufficient credibility. Another category of ULCF assessment method includes the stress triaxiality-associated prediction formulae and micro-damage mechanisms-based damage models, such as the large-range stress triaxiality-adaptive ductile fracture prediction model [26], the continuous damage model (CDM) [27] based on the continuum damage mechanisms, and the cyclic void growth model (CVGM) [28] developed from the void growth theory. These methods can take into account the influence of stress triaxiality on the ductile damage of materials, which are logically clear and suitable for precise ULCF evaluation under complex loading conditions. Nevertheless, the computation of the stress triaxiality needs very refined numerical simulation with solid elements, wherein the mesh size should be set to be consistent with the material characteristic length (usually 0.2-0.4mm for commonly used steel [2, 29-30]). The great discrepancy between the structural dimensions and the mesh size of the refined solid elements imposes great computational burden. Thus, the ULCF assessment is difficult to be popularized in practical engineering.

Due to the fatality of LI and ULCF, steel bridges constructed in seismically active areas should take both failure modes into account in their seismic design calculations. However, as mentioned above, such a seismic design process is difficult to apply in practical engineering because of the high computational costs involved in ULCF assessment. Currently, there is no appropriate approach available to efficiently process the seismic design. To this end, this paper proposed a simplified seismic design method that can avoid the burdensome ULCF calculations. Focusing on the damage occurrence priority of the two failure modes, the proposed method assumes that the ULCF assessment can be exempted by constructing piers with the failure occurrence priority of LI. Taking the widely used box-section single column steel pier as an example, the implementation and the credibility of the proposed method were illustrated. First, 90 piers with different structural parameters, representative of practical engineering applications, were designed. Then, based on a series of numerical work, the empirical formulae for the limit states of the LI failure of piers, such as the critical displacement and critical load, were fitted. After that, the ULCF assessment of piers under a hypothetical cyclic loading protocol were conducted to determine the damage occurrence priority. The seismic behavior of steel piers was also discussed to explain the mechanisms of different failure occurrence orders. Finally, dynamic analyses with real seismic wave inputs were conducted to verify the credibility of the proposed seismic design method.

2. Failure assessment methods for LI and ULCF

2.1. LI

Fig. 1 shows a typical hysteretic curve of a single-column steel pier under a constant axial load P and lateral cyclic displacement δ. In this figure, H represents the horizontal bearing capacity and the solid line indicates the hysteresis envelope. (δ_m, H_m) represents the peak point of the bearing capacity, and (δ_{95}, H_{95}) signifies the critical state where the bearing capacity begins to drop sharply. The entire envelope can be divided into three stages according to the structural mechanical degradation: In stage I, the structure is in the elastic and strengthening stage when the top displacement is less than δ_m, and no stiffness deterioration occurs; in stage II, its bearing capacity and stiffness begin to deteriorate slightly when the top displacement is between δ_m and δ_{95}; in stage III, the bearing capacity and stiffness start to degrade significantly when the lateral displacement δ exceeds δ_{95}.

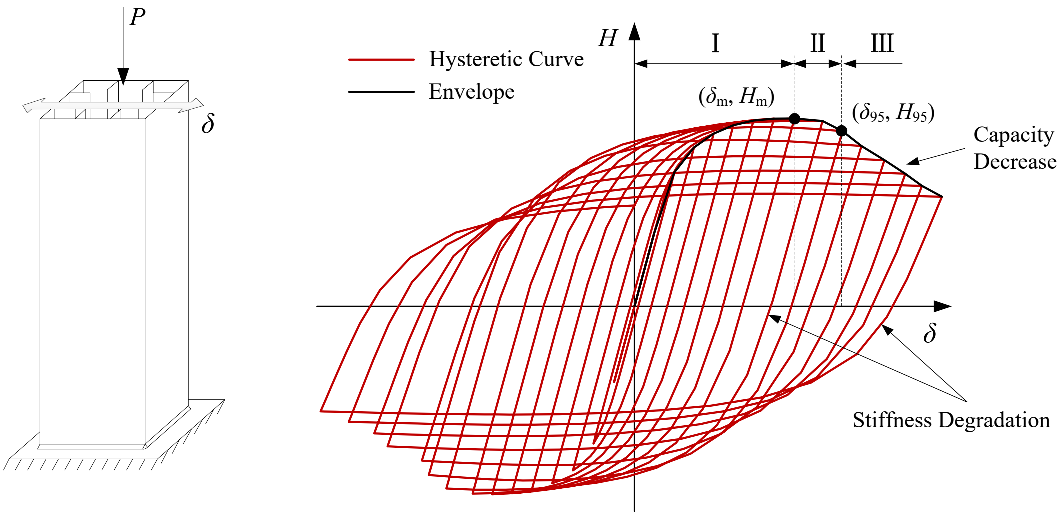

Fig. 1 Typical hysteretic curve of the single-column pier under cyclic lateral loads

Ge et al. summarized the experimental and theoretical results, and suggested the point (δ_{95}, H_{95}) that reduces to 95% of the peak bearing capacity as the critical state of LI [13]. Usami et al. conducted a series of tests and numerical analyses on the seismic performance of steel piers, and found that after reaching a certain critical state, the buckling instability of the structure initiates, and the bearing capacity begins to degrade rapidly, which leads to the final failure [31]. Generally, points (δ_m, H_m) and (δ_{95}, H_{95}) are always accepted as the vital limit state points for evaluating the seismic performance of steel piers, and the point (δ_{95}, H_{95}) is regarded as the LI damage initiation point [31-32].

2.2. ULCF

Under cyclic loading, complex and multidimensional stress states are involved in the vulnerable sites of piers. As mentioned above, among the two categories of assessment methods, the multi-dimensional methods that could take into account the effect of stress triaxiality can have a better interpretation for the ULCF fracture mechanism of the metal. Credible ULCF predictions can be obtained through precise material parameter calibration. The CVGM [28], which is developed from the micro-void growth mechanism, is a typical example. Applications of CVGM on different steel connections and steel piers for ductile fracture prediction have confirmed its feasibility and serviceability [33-37]. In this study, the CVGM was selected as a reference for initial cracking life assessment of steel piers.

The main content of this method includes a nonnegative cyclic void growth index VGI_{cyclic} and a cyclic void capacity index $VGI_{\text{cyclic}}^{\text{critical}}$, which are formulated as follows:

$$VGI_{\text{cyclic}} = \sum_{\text{tensile}} \int_{\varepsilon_1}^{\varepsilon_2} \exp\left(|1.5T|\right) \mathrm{d}\varepsilon_{\mathrm{p}} - \sum_{\text{compressive}} \int_{\varepsilon_1}^{\varepsilon_2} \exp\left(|1.5T|\right) \mathrm{d}\varepsilon_{\mathrm{p}} \geq 0 \tag{1}$$

$$VGI_{\text{cyclic}}^{\text{critical}} = \eta \cdot \exp\left(-\lambda \varepsilon_{\mathrm{p}}^{\text{accumulated}}\right) \tag{2}$$

where the upper and lower limits of Eq. (1), ε_1 and ε_2, are the equivalent plastic strains at the beginning and end of each tensile or compressive cycle, respectively; T is derived by the ratio of hydrostatic pressure σ_m and mises stress σ_{eq}, termed as stress triaxiality; $\mathrm{d}\varepsilon_{\mathrm{p}}=\sqrt{(2/3)\mathrm{d}\varepsilon_{ij}^{\mathrm{p}}\mathrm{d}\varepsilon_{ij}^{\mathrm{p}}}$ denotes the equivalent plastic strain; η and λ are two material constants governing the material toughness and damage degradation, respectively. It is assumed that ULCF fractures occurs when $VGI_{\text{cyclic}} \geq VGI_{\text{cyclic}}^{\text{critical}}$. According to our previous study [23], the two constants of Q345qC steel are taken as η=2.03 and λ=0.10, respectively.

3. Pier structure and FE model

3.1. Steel pier

The single-column steel pier with a stiffened box section was selected as the research object in this study. Its outline and sectional details are shown in Fig. 2. Piers are made of Q345qC steel, which is a commonly used material in Chinese steel bridges; full penetrating weld process is applied to connect the stiffening plates and the end plates, and the yellow part shown in Fig. 2 represents the welded area. The main structural parameters of steel piers include the slenderness ratio λ_B, width-to-thickness ratio R_R, axial compression ratio P/P_y and the relative stiffness of the stiffeners. The λ_B and R_R calculations are expressed as [38]:

$$\lambda_{\mathrm{B}} = \frac{2h}{r}\frac{1}{\pi}\sqrt{\frac{\sigma_{\mathrm{y}}}{E}} \tag{3}$$

$$R_{\mathrm{R}} = \frac{B}{t}\sqrt{\frac{12\left(1-\nu^2\right)}{4\pi^2 n_{\mathrm{r}}^2}}\sqrt{\frac{\sigma_{\mathrm{y}}}{E}} \tag{4}$$

where h is the height of the piers, r denotes the radius of gyration in the deformed direction, B is the width of the flange, t is the thickness of the stiffening plate, n_r is the number of regions divided by stiffeners in the stiffening plate, $\nu = 0.3$ is the Poisson's ratio. Stipulated by the codified standards [18], the relative stiffness of the stiffener is defined and limited as:

$$\begin{cases} \dfrac{\gamma}{\gamma^*} = \dfrac{EI_{\mathrm{l}}}{BD'\gamma^*} \geq 1 \\ \gamma_{\mathrm{t}} = \dfrac{EI_{\mathrm{t}}}{BD'} \geq \dfrac{1+n_{\mathrm{r}}\gamma}{4\left(a/B\right)^3} \end{cases} \tag{5}$$

$$\frac{b_{\mathrm{s}}}{t_{\mathrm{s}}} \leq 12\sqrt{\frac{345}{\sigma_{\mathrm{y}}}} \tag{6}$$

where γ and γ_t denote the relative stiffness of the longitudinal stiffeners and diaphragms, respectively; I_l and I_t are the bending moments of inertia of a single longitudinal stiffener and a single diaphragm, respectively; D' is the bending stiffness of the steel plates per unit width; a is the spacing of the transverse partitions; t_s and b_s are the thickness and width of the vertical stiffener, respectively; γ^* represents the optimal stiffness ratio of stiffeners, which is defined as:

$$\gamma^{*}=\begin{cases}\dfrac{1}{n_r}\left[4n_r^{2}\left(1+n_r\dfrac{b_s t_s}{Bt}\right)\alpha^{2}-\left(\alpha^{2}+1\right)^{2}\right] & \alpha\le\sqrt[4]{1+n_r\gamma}\\ \dfrac{1}{n_r}\left\{\left[2n_r^{2}\left(1+n_r\dfrac{b_s t_s}{Bt}\right)\alpha^{2}-1\right]^{2}-1\right\} & \alpha>\sqrt[4]{1+n_r\gamma}\end{cases} \tag{7}$$

where $\alpha = a/B$. According to the ranges of the structural parameter values in practical projects, $0.25 \le \lambda_B \le 0.50$, $0.30 \le R_R \le 0.50$ and $0.10 \le P/P_y \le 0.30$ were selected. Table 1 presents the geometric characteristics of the designed 90 piers, using the free combination of these three parameter ranges. Each row of data listed in this table represents three pier working conditions ($P/P_y = 0.1$, 0.2, and 0.3). Some constant variables, such as flange width B (0.45m), sectional aspect ratio W/B (1.0), diaphragm spacing a (0.45m), and optimal stiffness ratio γ/γ^* (1.5), are not included in Table 1.

Table 1
Geometric dimensions and structural parameters of piers

No.	h(m)	λ_B	R_R	t(m)	t_s(m)	b_s(m)
S25-30	1.61	0.250	0.298	0.0110	0.0110	0.083
S25-35	1.63	0.250	0.349	0.0094	0.0094	0.073
S25-40	1.64	0.250	0.395	0.0083	0.0083	0.066
S25-45	1.65	0.250	0.449	0.0073	0.0073	0.060
S25-50	1.66	0.250	0.504	0.0065	0.0065	0.055
S30-30	1.95	0.302	0.298	0.0110	0.0110	0.083
S30-35	1.96	0.301	0.349	0.0094	0.0094	0.073
S30-40	1.98	0.301	0.395	0.0083	0.0083	0.066
S30-45	2.00	0.302	0.449	0.0073	0.0073	0.060
S30-50	2.00	0.301	0.504	0.0065	0.0065	0.055
S35-30	2.26	0.350	0.298	0.0110	0.0110	0.083
S35-35	2.29	0.351	0.349	0.0094	0.0094	0.073
S35-40	2.30	0.350	0.395	0.0083	0.0083	0.066
S35-45	2.31	0.349	0.449	0.0073	0.0073	0.060
S35-50	2.31	0.348	0.504	0.0065	0.0065	0.055
S40-30	2.59	0.402	0.298	0.0110	0.0110	0.083
S40-35	2.62	0.402	0.349	0.0094	0.0094	0.073
S40-40	2.63	0.400	0.395	0.0083	0.0083	0.066
S40-45	2.65	0.401	0.449	0.0073	0.0073	0.060
S40-50	2.65	0.399	0.504	0.0065	0.0065	0.055
S45-30	2.91	0.451	0.298	0.0110	0.0110	0.083
S45-35	2.95	0.452	0.349	0.0094	0.0094	0.073
S45-40	2.97	0.452	0.395	0.0083	0.0083	0.066
S45-45	2.99	0.452	0.449	0.0073	0.0073	0.060
S45-50	3.00	0.451	0.504	0.0065	0.0065	0.055
S50-30	3.16	0.490	0.298	0.0110	0.0110	0.083
S50-35	3.19	0.490	0.349	0.0094	0.0094	0.073
S50-40	3.21	0.490	0.395	0.0083	0.0083	0.066
S50-45	3.25	0.491	0.449	0.0073	0.0073	0.060
S50-50	3.25	0.490	0.482	0.0065	0.0065	0.055

Note: Taking S25-30 as an example, S indicates steel pier; 25 means $\lambda_B = 0.25$ and 30 represents $R_R = 0.30$.

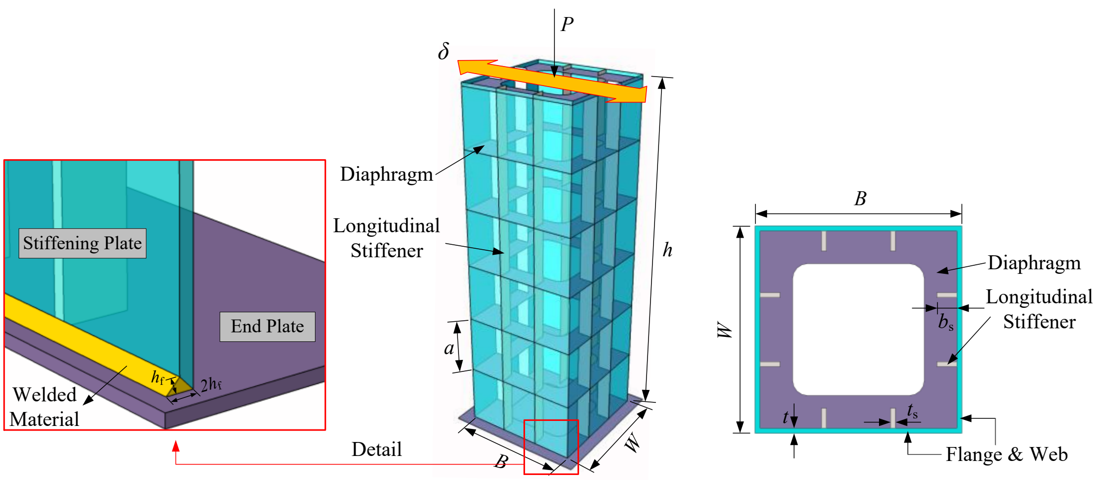

Fig. 2 Schematic diagram of steel pier

3.2. FE Model

The operation of CVGM requires the results of stress triaxiality, where local solid modelling is required, and the solid element size should be consistent with the characterized length L^* (0.2 mm) of Q345qC steel [28, 36]. Experimental investigations of steel piers have shown that the welded corners are the most vulnerable sites of ductile crack initiation [6, 10-12], which is the region where local refinement is imposed. Given the significant difference between the characteristic length L^* and the structural dimensions of piers, the two-level zooming sub-model strategy was adopted to pursue a cost-effective simulation process.

The FE simulation process is carried out on the ABAQUS 6.14-4 platform. As illustrated in Fig. 3, the first-level zooming consists of the global model and the sub1 model; the second-level zooming consists of the sub1 model and the sub2 model. In the global model, the pier bottom is completely fixed and the basic geometric content of the pier structure is included. The whole model is modelled by the 4-node reduced integral shell element S4R, except that a short range at the top is simulated by the 2-node linear beam element B31 to transfer the horizontal cyclic deformation δ and axial force P. The multi-point coupling (MPC) is exerted between shell elements and beam elements for consolidating their boundary. The followed sub1 model, representing a part of the bottom of the pier, is entirely modelled by the 8-node reduced integral brick element C3D8R, in which the geometry of the weld joints is reflected. Owing to the restriction of element characteristics, at least four layers of solid elements is divided along the thickness direction of the plates to cater to the change in bending stress [39], as depicted in Fig.3(b). The final sub2 model only contains a weld corner of the sub1 model, which is also modelled by solid element C3D8R. The mesh size of the solid element in the vulnerable sites corresponds to the material characteristic length L^*, controlled at 0.2 mm [30]. These three models present a progressive relationship towards the refined simulation of weld toe. For each sub-model, the displacement solution generated from the previous-level model is converted to the enforced displacement acted on its exposed surfaces as the driven load. Weld details are ignored in the global model because that it has no effect on the nodal displacement of the driven surface between the global model and the sub1 model. To ensure the reliability of the stress and strain results, the exposed surfaces of each sub-model are kept at least 1.5 times the width or thickness away from the areas of concern, such as 1.5B or 1.5t shown in Fig. 3(b, c). The Chaboche hybrid hardening constitutive model is applied for the accurate expression of cyclic metal plasticity. The constitutive parameters of Q345qC steel have been calibrated in the previous study [30] and are listed in Table 2.

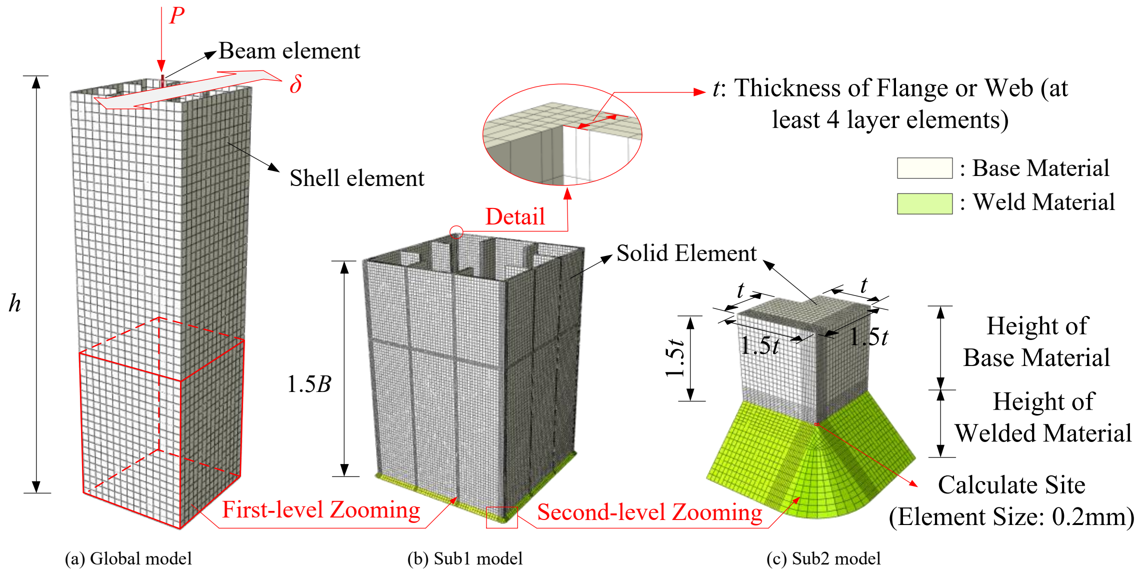

Fig. 3 Schematic diagram of FE model

Table 2
Parameters of the Chaboche constitutive model of Q345qC steel [30]

Material	$\sigma\|_0$(MPa)	Q_∞(MPa)	b_{iso}	C_1(MPa)	γ_1	C_2(MPa)	γ_2	C_3(MPa)	γ_3
Base Material	354.10	13.2	0.6	44373.7	523.8	9346.6	120.2	946.1	18.7
Weld Material	428.45	17.4	0.4	12752.3	160.0	1111.2	160.0	630.5	26.0

Note: $\sigma|_0$ is initial yield stress; Q_∞ is the maximum variation of yield surface; b_{iso} is the change ratio of the yield surface with the plastic strain; C_1, C_2 and C_3 are initial kinematic moduli of the three back stress components; γ_1, γ_2 and γ_3 are kinematic moduli of the three back stress components.

3.3. Experimental verification

Three cyclic loading tests that were conducted in our previous experimental investigation [10, 40] are applied here to examine the validity of the above analytical system. Geometrics of these three piers are listed in Table 3. Cyclic displacement was set along the 45 ° direction of the main sectional axis, with the loading protocol of displacement amplitude increasing by 0.5 times of δ_y (the yield displacement) per cycle. The weld corner at pier bottom was repeatedly pulled and compressed under this loading condition, making it the vulnerable site to fracture. The damage phenomena of these three piers were basically the same: micro cracks were firstly observed at the weld corner and propagated stably under the subsequent cyclic loads, followed by the sudden fracture and accompanied with the slight curvature of steel plates, as shown in Fig. 5(b). See references [10, 40] for more experimental details.

Table 3
Geometric dimensions and structural parameters of pier specimens [10, 40]

No.	H(m)	B(m)	W/B	λ_B	R_R	P/P_y	a(m)	t(m)	t_s(m)	b_s(m)
SP-1	2.00	0.45	1.00	0.32	0.467	0.2	0.45	0.008	0.008	0.049
SP-2	1.25	0.32	1.00	0.31	0.332	0.2	0.16	0.0074	0.0074	0.039
SP-3	0.65	0.20	1.00	0.29	0.311	0.2	0.10	0.0074	0.0074	0.034

The purpose of using the two-level zooming analytical system in this paper is to judge the damage occurrence sequence of the two failure modes of steel bridge piers. Thus, the experimental verification of the analytical system starts from these two parts. Comparations were made between the numerical and experimental hysteretic curves of pier specimens to verify the reliability of LI assessment, as shown in Fig. 4. The maximum relative errors between the experimental and numerical results are 7.6%, 10.9%, and 22.6% for SP-1, SP-2 and SP-3, respectively. The larger error shown in specimen SP-3 may be caused by the sliding between the fixture and pier base, as illustrated in the previous research [10]. Other key properties, such as the structural stiffness revolution and skeleton curve shape, are in good agreement with the test, which supports the reliability of the analytical system for LI assessment. Besides, the experimental ULCF fracture initiation results N_e and the cracking life N_p predicted by CVGM are presented in Table 4, in which only slight errors exist. The contour plot of the equivalent plastic strain of the sub2 model shown in Fig. 5 reveals that the calculated element has the highest plastic concentration, corresponding to the first occurrence position of ULCF cracks, which indicates the acceptable convincement of applying the two-level zooming strategy for ULCF assessment.

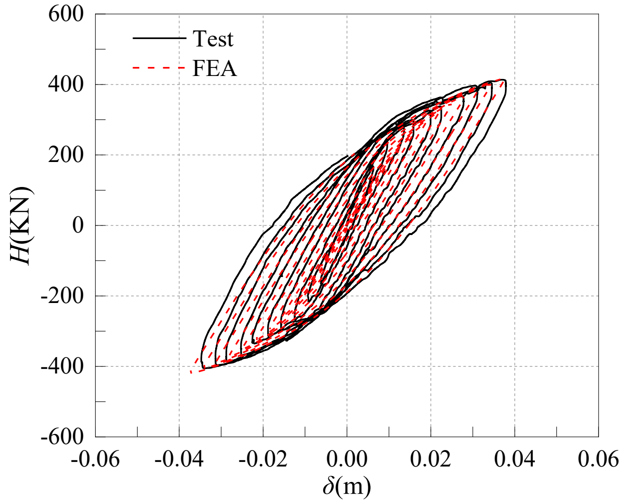

(a) SP-1

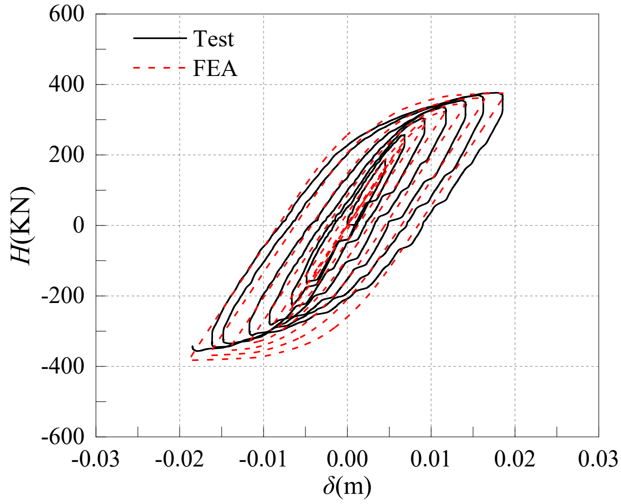

(b) SP-2

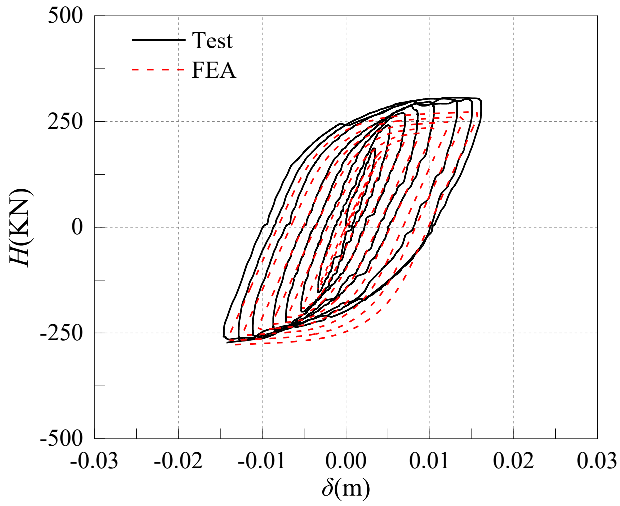

(c) SP-3

Fig. 4 Comparison of hysteretic curves obtained from tests and numerical analyses

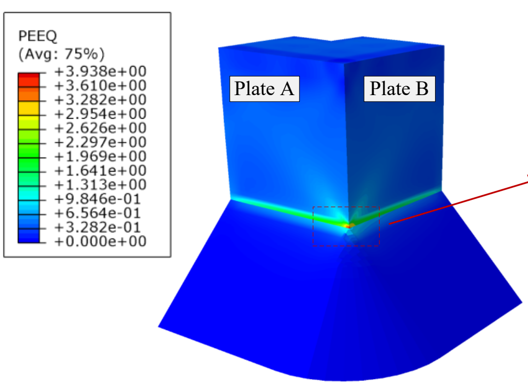

(a) Contour plot of equivalent plastic strain

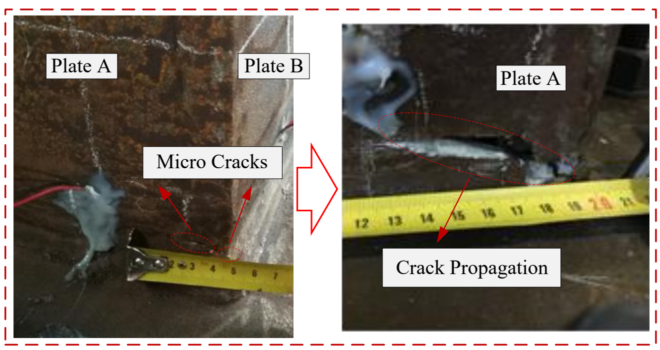

(b) ULCF initiation observed in tests

Fig. 5 Plastic strain accumulation and ULCF initiation at the weld corner

Table 4
Comparation of experimental and numerical ULCF life

Specimen	N_e (Cycle)	N_p (Cycle)	Relative Error
SP-1	8	7	12.5%
SP-2	7	8	14.3%
SP-3	7	7	0.0%

4. Quasi-static analysis

4.1. Limit states

As illustrated earlier in Section 2.1, H_m, δ_m, and δ_{95} are the vital limit state points for evaluating the LI failure of steel piers, which also serve as the intermediate variables for the subsequent failure sequence judgment in this study. Elastoplastic analyses were carried out for the designed 90 piers with the load protocol shown in Fig. 6(a) [41-42] to acquire these limit states. Results are shown in Tables 5-7.

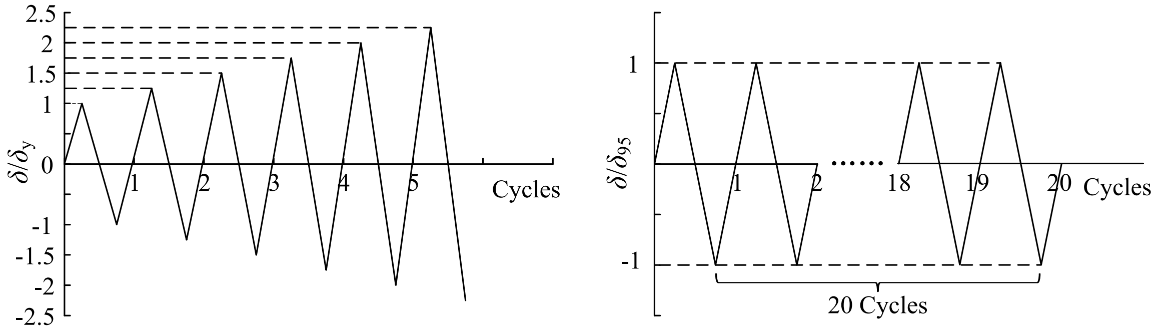

(a) Used for limit state analyses (b) Used for damage priority determination

Fig. 6 Loading protocols

Table 5
Limit states of box section steel piers (P/P_y=0.10)

No.	λ=0.25			No.	λ=0.30			No.	λ=0.35		
	H_m/H_y	δ_m/δ_y	δ_{95}/δ_y		H_m/H_y	δ_m/δ_y	δ_{95}/δ_y		H_m/H_y	δ_m/δ_y	δ_{95}/δ_y
S25-30	2.03	4.74	5.88	S30-30	2.02	4.95	5.87	S35-30	2.00	4.78	5.62
S25-35	1.93	4.26	5.15	S30-35	1.91	4.12	4.86	S35-35	1.89	3.96	4.58
S25-40	1.87	3.87	4.47	S30-40	1.85	3.71	4.26	S35-40	1.83	3.48	4.08
S25-45	1.80	3.14	3.61	S30-45	1.79	2.97	3.48	S35-45	1.77	2.89	3.40
S25-50	1.74	3.06	3.43	S30-50	1.72	2.89	3.24	S35-50	1.71	2.80	3.13
No.	λ=0.40			No.	λ=0.45			No.	λ=0.50		
	H_m/H_y	δ_m/δ_y	δ_{95}/δ_y		H_m/H_y	δ_m/δ_y	δ_{95}/δ_y		H_m/H_y	δ_m/δ_y	δ_{95}/δ_y
S40-30	1.97	4.59	5.28	S45-30	1.95	4.42	5.17	S50-30	1.94	4.03	5.01
S40-35	1.87	3.71	4.43	S45-35	1.86	3.74	4.17	S50-35	1.83	3.57	4.18
S40-40	1.81	3.40	3.92	S45-40	1.79	3.21	3.79	S50-40	1.77	3.21	3.71
S40-45	1.75	2.80	3.30	S45-45	1.73	2.72	3.25	S50-45	2.68	3.18	1.71
S40-50	1.69	2.71	3.02	S45-50	1.67	2.66	2.99	S50-50	1.69	2.71	3.02

Table 6
Limit states of box section steel piers (P/P_y=0.20)

No.	λ=0.25			No.	λ=0.30			No.	λ=0.35		
	H_m/H_y	δ_m/δ_y	δ_{95}/δ_y		H_m/H_y	δ_m/δ_y	δ_{95}/δ_y		H_m/H_y	δ_m/δ_y	δ_{95}/δ_y
S25-30	2.18	4.80	5.66	S30-30	2.16	4.48	5.35	S35-30	2.14	4.40	5.39
S25-35	2.08	4.12	4.79	S30-35	2.06	3.93	4.54	S35-35	2.03	3.82	4.39
S25-40	2.01	3.71	4.28	S30-40	1.99	3.57	4.09	S35-40	1.96	3.50	3.96
S25-45	1.95	3.23	3.62	S30-45	1.93	3.15	3.49	S35-45	1.91	3.06	3.42
S25-50	1.87	3.15	3.44	S30-50	1.86	3.06	3.32	S35-50	1.83	2.97	3.24
No.	λ=0.40			No.	λ=0.45			No.	λ=0.50		
	H_m/H_y	δ_m/δ_y	δ_{95}/δ_y		H_m/H_y	δ_m/δ_y	δ_{95}/δ_y		H_m/H_y	δ_m/δ_y	δ_{95}/δ_y
S40-30	2.10	4.25	4.92	S45-30	2.07	4.12	4.79	S50-30	2.05	3.96	4.55
S40-35	2.00	3.63	4.27	S45-35	1.98	3.67	4.04	S50-35	1.94	3.46	4.03
S40-40	1.93	3.40	3.85	S45-40	1.90	3.30	3.74	S50-40	1.88	3.14	3.63
S40-45	1.88	2.97	3.35	S45-45	1.86	2.89	3.31	S50-45	1.83	2.80	3.27
S40-50	1.81	2.80	3.09	S45-50	1.78	2.71	3.01	S50-50	1.78	2.80	3.11

Table 7
Limit states of box section steel piers (P/P_y=0.30)

No.	λ=0.25			No.	λ=0.30			No.	λ=0.35		
	H_m/H_y	δ_m/δ_y	δ_{95}/δ_y		H_m/H_y	δ_m/δ_y	δ_{95}/δ_y		H_m/H_y	δ_m/δ_y	δ_{95}/δ_y
S25-30	2.36	4.56	5.42	S30-30	2.33	4.41	5.11	S35-30	1.96	2.97	3.21
S25-35	2.24	4.06	4.64	S30-35	2.22	3.86	4.42	S35-35	2.18	3.74	4.28
S25-40	2.17	3.74	4.19	S30-40	2.14	3.58	4.01	S35-40	2.11	3.50	3.90
S25-45	2.11	3.35	3.63	S30-45	2.08	3.15	3.50	S35-45	2.05	3.10	3.40
S25-50	2.02	3.17	3.43	S30-50	1.99	3.01	3.30	S35-50	1.96	2.97	3.21
No.	λ=0.40			No.	λ=0.45			No.	λ=0.50		
	H_m/H_y	δ_m/δ_y	δ_{95}/δ_y		H_m/H_y	δ_m/δ_y	δ_{95}/δ_y		H_m/H_y	δ_m/δ_y	δ_{95}/δ_y
S40-30	2.25	4.16	4.74	S45-30	2.20	3.96	4.60	S50-30	2.20	3.93	4.46
S40-35	2.14	3.65	4.15	S45-35	2.11	3.58	3.99	S50-35	2.06	3.48	3.94
S40-40	2.07	3.41	3.81	S45-40	2.02	3.32	3.69	S50-40	1.99	3.23	3.60
S40-45	2.01	2.97	3.34	S45-45	1.98	2.97	3.32	S50-45	1.94	2.93	3.27
S40-50	1.92	2.88	3.14	S45-50	1.88	2.79	3.04	S50-50	1.88	2.80	3.13

From Tables 5-6, it is obvious that higher piers with thinner plates are more prone to suffering LI failure. The statistical analysis software IBM SPSS Statistics [43] was used to perform the nonlinear multivariate regression of the empirical limit state formulae of piers. The fitted empirical formulae are expressed as Eq. (8):

$$\begin{cases} \dfrac{H_m}{H_y} = 1.163\left(1+\dfrac{N}{N_y}\right)^{0.819} R_R^{\ 0.384}\lambda_B^{\ -0.1}\left(\lambda_s^{'}\right)^{-0.641}, \quad \left(R^2=0.991\right) \\ \dfrac{\delta_m}{\delta_y} = 1.267\left(1+\dfrac{N}{N_y}\right)^{-0.121} R_R^{\ -10.068}\lambda_B^{\ -0.231}\left(\lambda_s^{'}\right)^{8.768}, \quad \left(R^2=0.965\right) \\ \dfrac{\delta_{95}}{\delta_y} = 1.328\left(1+\dfrac{N}{N_y}\right)^{-0.347} R_R^{\ -7.92}\lambda_B^{\ -0.248}\left(\lambda_s^{'}\right)^{6.616}, \quad \left(R^2=0.979\right) \end{cases} \tag{8}$$

where, $\lambda_s^{'}$ is the modified slenderness ratio parameter of the stiffener defined by Ge et al. [38]; R^2 is the determinant coefficient. A value of R^2 closer to 1 indicates a better fit between the data and model. These formulae work for piers with stiffened box section within the parameter case $0.25 \le \lambda_B \le 0.50$, $0.30 \le R_R \le 0.50$, $0.10 \le P/P_y \le 0.30$ and γ/γ^*=1.5, providing an empirical reference for quick evaluation of LI damage of piers. Fig. 7 depicts the empirical curves, wherein the discrete points are the FE results listed in Tables 5-7. The agreement between the numerical data and regression curve suggests the high credibility of the empirical formulae.

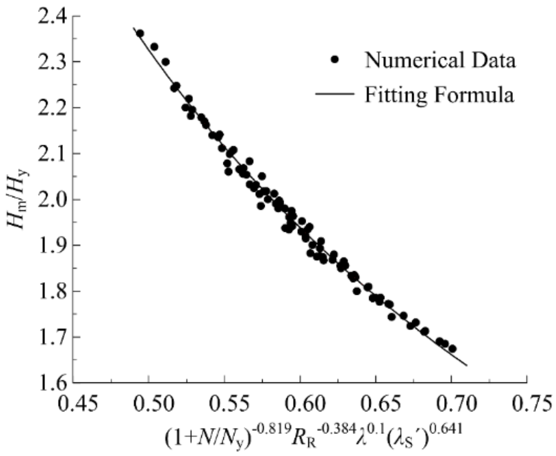

(a) H_m/H_y

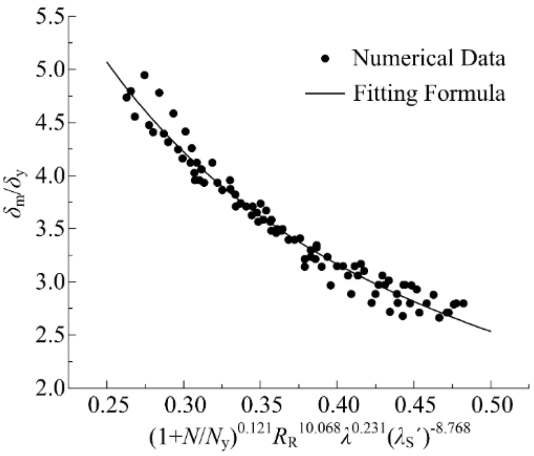

(b) δ_m/δ_y

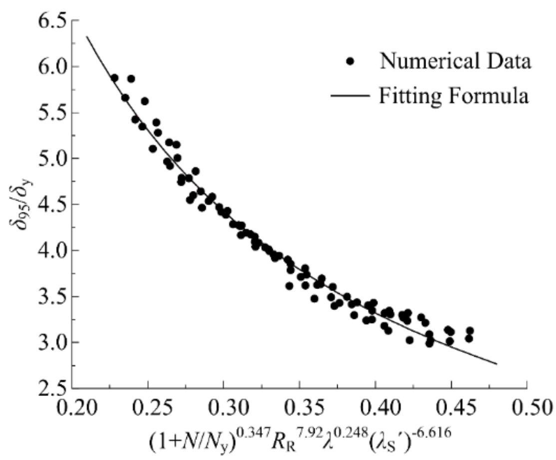

(c) δ_{95}/δ_y

Fig. 7 Fitting results of the regression formula for the limit state values

4.2. Damage occurrence priority

Given that the ULCF life is usually less than 20 loading cycles [1-2], the constant amplitude cyclic loading protocol shown in Fig. 6(b), which is characterized by the displacement amplitude of each pier's δ_{95} and the total loading cycle of 20, was adopted as the loading strategy for determining the failure occurrence priority of LI and ULCF. And there is a logical explanation for this selection. If a steel pier does not experience ULCF failure by the end of loading, that is, the structure is subjected to the LI failure for 20 times without undergoing the ULCF failure, it can be considered that the damage occurrence priority is LI. Otherwise, the damage occurrence priority is ULCF. Since the LI calculation is necessary whether LI or ULCF occurs first, this loading protocol is considered conservative to determine the damage priorities. Tables 8-10 list the estimated ULCF life of the 90 piers, in which "-" indicates that no ULCF fracture occurs until the end of the load. Furthermore, a dotted polyline is attached to each table to have a more intuitive distinguishment of different damage sequence.

Table 8
Predicted ULCF life versus structural parameters under P/P_y=0.10 (Unit: cycle)

R_R \ λ	0.25	0.30	0.35	0.40	0.45	0.50
0.50	-	-	-	-	-	-
0.45	-	-	-	-	-	-
0.40	5.78	-	-	-	-	-
0.35	0.77	0.73	1.76	1.77	2.79	2.81
0.30	0.65	0.65	0.65	0.69	0.73	0.71

Table 9
Predicted ULCF life versus structural parameters under P/P_y=0.20 (Unit: cycle)

R_R \ λ	0.25	0.30	0.35	0.40	0.45	0.50
0.50	-	-	-	-	-	-
0.45	-	-	-	-	-	-
0.40	-	-	-	-	-	-
0.35	2.76	2.81	0.71	4.80	-	-
0.30	0.75	1.67	1.69	1.81	2.76	3.77

Table 10
Predicted ULCF life versus structural parameters under P/P_y=0.30 (Unit: cycle)

R_R \ λ	0.25	0.30	0.35	0.40	0.45	0.50
0.50	-	-	-	-	-	-
0.45	-	-	-	-	-	-
0.40	-	-	-	-	-	-
0.35	-	-	-	-	-	-
0.30	2.79	2.77	-	-	-	-

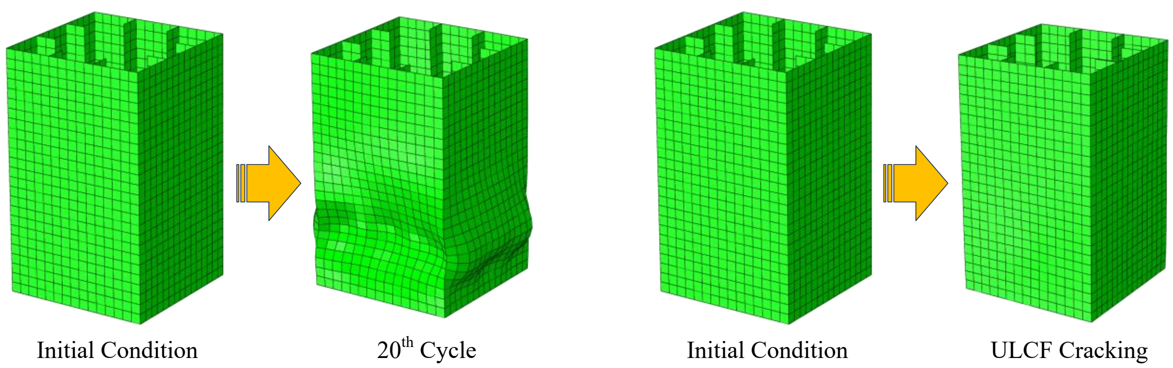

(a) S50-40P20 (thin-walled) (b) S25-35P20 (thick-walled)

Fig. 8 Deformation diagram

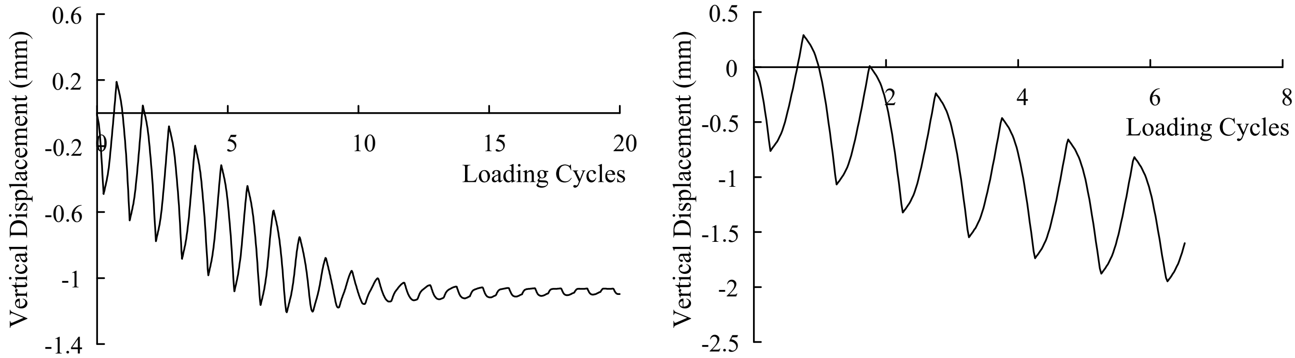

(a) S50-40P20 (thin-walled)

(b) S25-35P20 (thick-walled)

Fig. 9 Plastic displacement history of weld corner

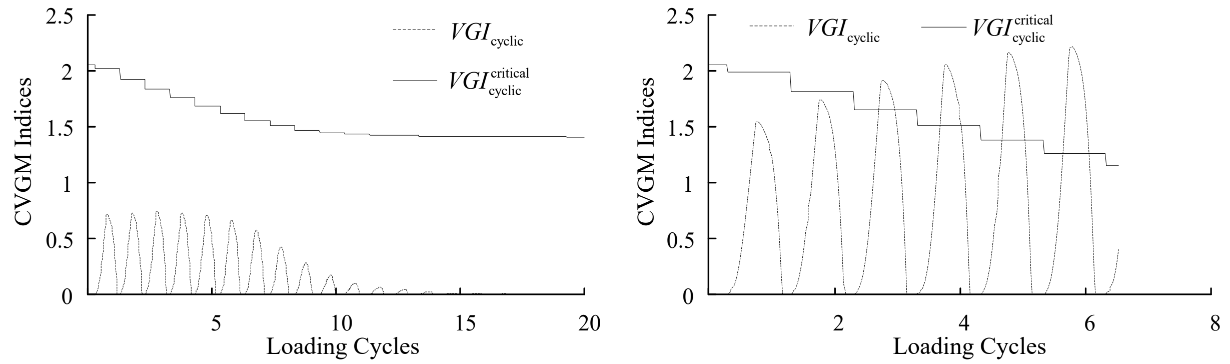

(a) S50-40P20 (thin-walled)

(b) S25-35P20 (thick-walled)

Fig. 10 ULCF calculation process

It is obvious from the data presented in the tables that shorter piers with thicker plates are more inclined to ULCF damage, which is consistent with the qualitative relationship derived by Ge. et al. based on pier tests [11]. Also, it is found that with the increase of P/P_y, the damage occurrence priority tends to be the LI failure. An insight into the ULCF assessment process indicates that for piers with the ULCF life of "-", the absence of ULCF failure is not caused by the limited loading cycles (only 20 cycles) of the loading assumption. As shown in Fig. 10(a), the cyclic void growth index VGI_{cyclic} seems never exceeds the cyclic void capacity index $VGI_{\text{cyclic}}^{\text{critical}}$. In other words, the ULCF failure will never occur. To have a better explanation of the mechanism of this phenomenon, the ULCF damage evolution is discussed with the LI damage aggravation. Taking piers S50-40 with P/P_y=0.20 (abbreviated as S50-40P20) and S25-35 with P/P_y =0.20 (abbreviated as S25-35P20) as the representatives of the two different failure priorities, the deformation diagram of the overall structure at the instant of ULCF initiation or the end of the load, as well as the plastic displacement history of the weld corner are depicted in Fig. 8 and Fig. 9, respectively. Fig. 10 also depicts the evolution of the cyclic void growth index VGI_{cyclic} and the cyclic void capacity index $VGI_{\text{cyclic}}^{\text{critical}}$ of the two piers. It is found that for the typical thin-walled member (S50-40P20), the LI damage is particularly dominant, indicated by the steeply curved flange and web (Fig. 8(a)). Moreover, with the accumulation of LI damage, the amplitude of plastic displacement at the weld corner gradually decreases (Fig. 9(a)). Thus, it is of a rational deduction that the cyclic displacement transmitted from the superstructure is concentrated at a local area of the flange or web and is no longer transmitted downward. Correspondingly, the repeated expansion and compression of micro-voids within the metal of weld corner slows down, resulting in the prolonged ULCF life (Fig. 10(a)). In contrast, for the thick-walled member (S25-35P20), due to the absence of LI damage (Fig. 8(b)), the amplitude of plastic displacement at the weld corner remains constant until the final fracture (Fig. 9(b)), resulting in the continuous damage of ULCF (Fig. 10(b)). Apparently, it is the deformation characteristics of the structure, which is the comprehensive reflection of the relative thickness (width-to-thickness ratio), bending tolerance (slenderness ratio) and the degree of compression (axial compression ratio), that determine the different deformation patterns and further control the failure priorities.

In practical engineering, the structural parameters of steel pier can be set following the derived damage priorities, by which the designed pier will be prone to suffering LI damage. Thus, it is unnecessary to perform the burdensome ULCF assessment, and the seismic design calculations can be simplified.

5. Dynamic analysis

The derived damage occurrence priority is based on the quasi-static analyses under the assumed load protocol. To verify its reliability and applicability, nonlinear dynamic time-history analyses of steel piers with real earthquake wave inputs were performed.

5.1. Seismic excitation

To ensure the coexistence of LI and ULCF damage during time-history analyses, the selected seismic excitation should be destructive. In this study, the Northridge earthquake recorded at the LDM station in 1994, the Chi Chi earthquake recorded at the Caotun station in 1999 and the Lushan earthquake recorded at the 51BXD station in 2013 were used as ground motion inputs. The LDM station of the Northridge earthquake is located on the hanging wall of the fault; the Caotun station of the Chi Chi earthquake is located in the northwest of the source, which is near the rupture surface of the fault and is located on the footwall of the fault; the 51BXD station of the Lushan earthquake is located in the northwest of the source and on the hanging wall of the fault. These three seismic records are typical near-field motions. Among them, the seismic waves recorded at the LDM and Caotun stations have obvious pulse effects, and the ground motion in the long period range is dominant. While for the Lushan earthquake recorded at the 51BXD station, its pulse effect is not obvious and the ground motion in the short-period range is dominant. The acceleration time histories of these three records are presented in Fig. 11, where a_g represents the ground acceleration and t represents time.

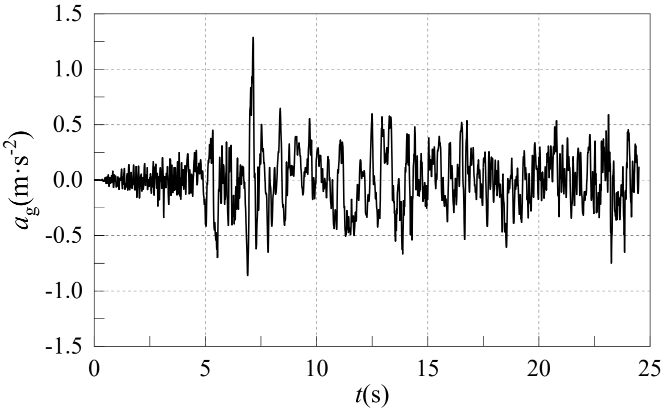

(a) the Chi Chi earthquake

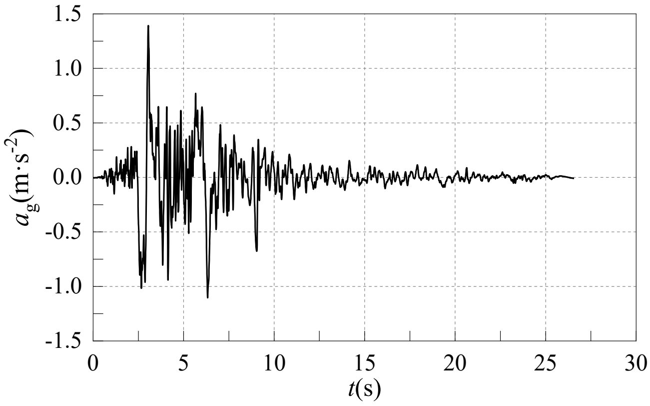

(b) the Northridge earthquake

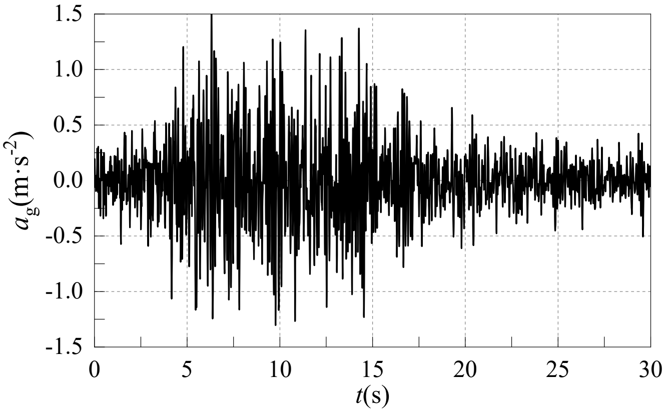

(c) the Lushan earthquake

Fig. 11 Seismic waves

5.2. Seismic performance of piers

Owing to the space limitation of the paper, only three piers, namely S40-45P20, S30-35P10, and S30-35P30, were applied as examples for validating the reliability of the derived damage occurrence priority. The structural parameters of these three piers are located near the dotted polylines attached in Tables 8-10 for the sake of effective verification. Results of the hysteresis curves and the CVGM indices evolution of these three piers under seismic excitations are presented in Figs. 12-14. Initiations of LI failure and ULCF failure are determined by the limit state point (δ_{95}, H_{95}) and CVGM criterion $VGI_{\text{cyclic}} \geq VGI_{\text{cyclic}}^{\text{critical}}$, respectively, which are marked in the figures. It is shown that the computed damage occurrence priorities are LI damage-dominant for piers S40-45P20 and S30-35P30, and ULCF damage-dominant for pier S30-35P10, indicating the good consistency with the damage occurrence listed in Tables. 8-10.

The dynamic analyses conducted in this paper were only examples to verify the reliability of the simplified seismic design method using the damage occurrence sequence. Due to the assumed loading protocol, the determination of whether ULCF checking is necessary, as discussed in this paper, is conservative. The piers prioritized for ULCF damage in this study may undergo LI damage before ULCF under actual seismic loading. However, piers designed using the simplified design method proposed in this paper are considered to be on the safer side under such a situation.

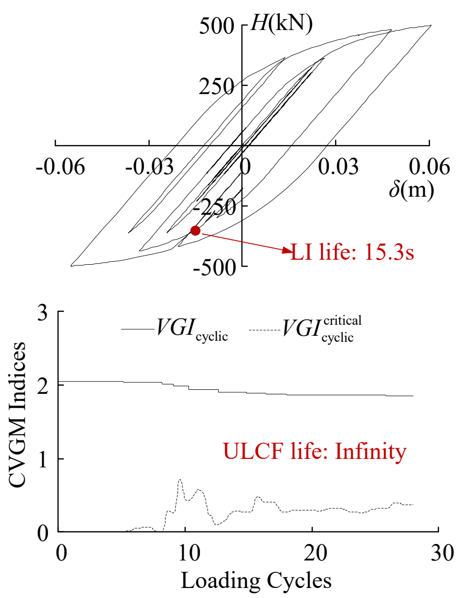

(a) S40-45P20

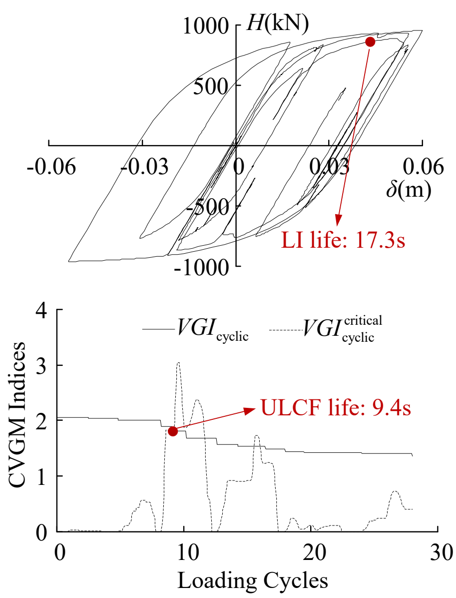

(b) S30-35P10

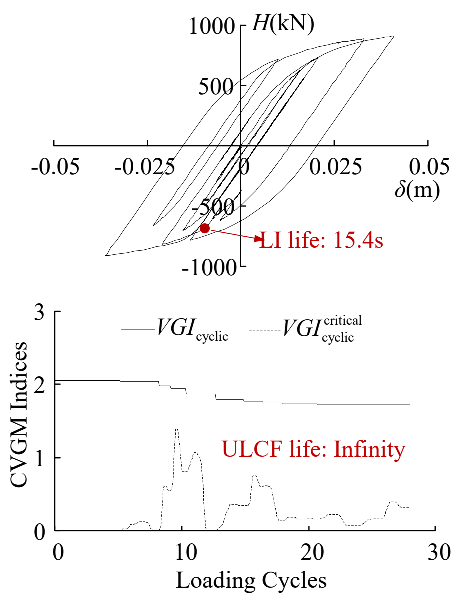

(c) S30-35P30

Fig. 12 Seismic performance of piers under Chi Chi earthquake

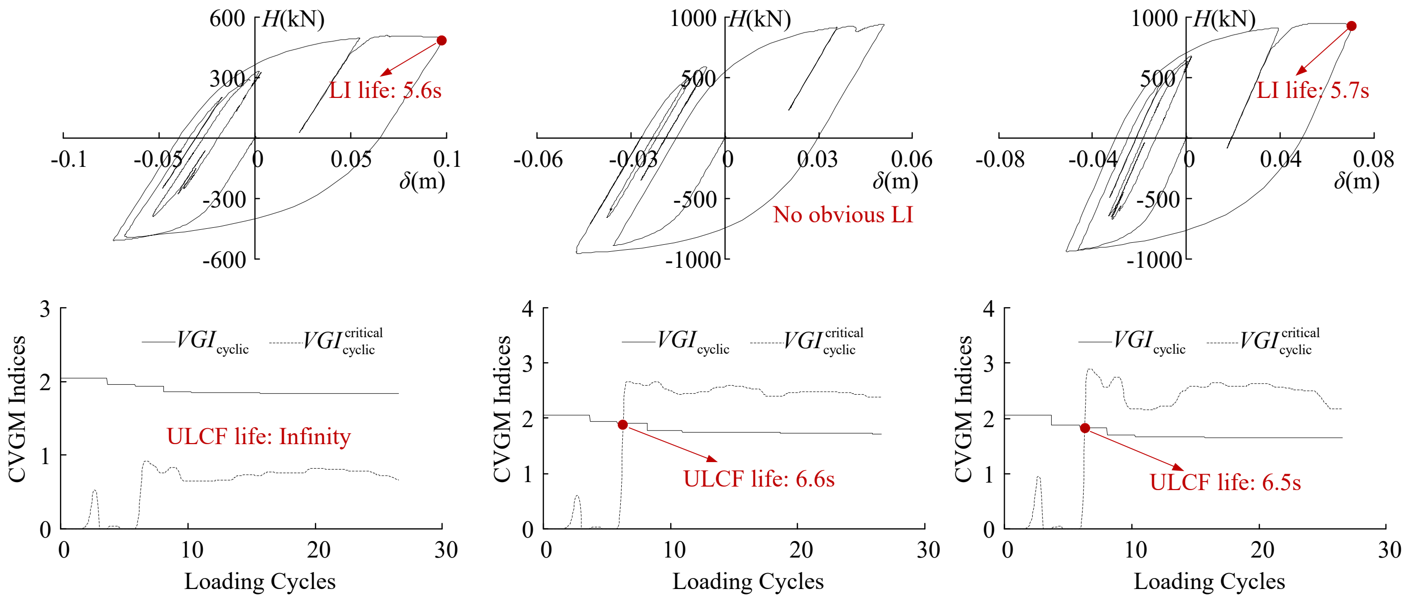

(a) S40-45P20 (b) S30-35P10 (c) S30-35P30

Fig. 13 Seismic performance of piers under Northridge earthquake

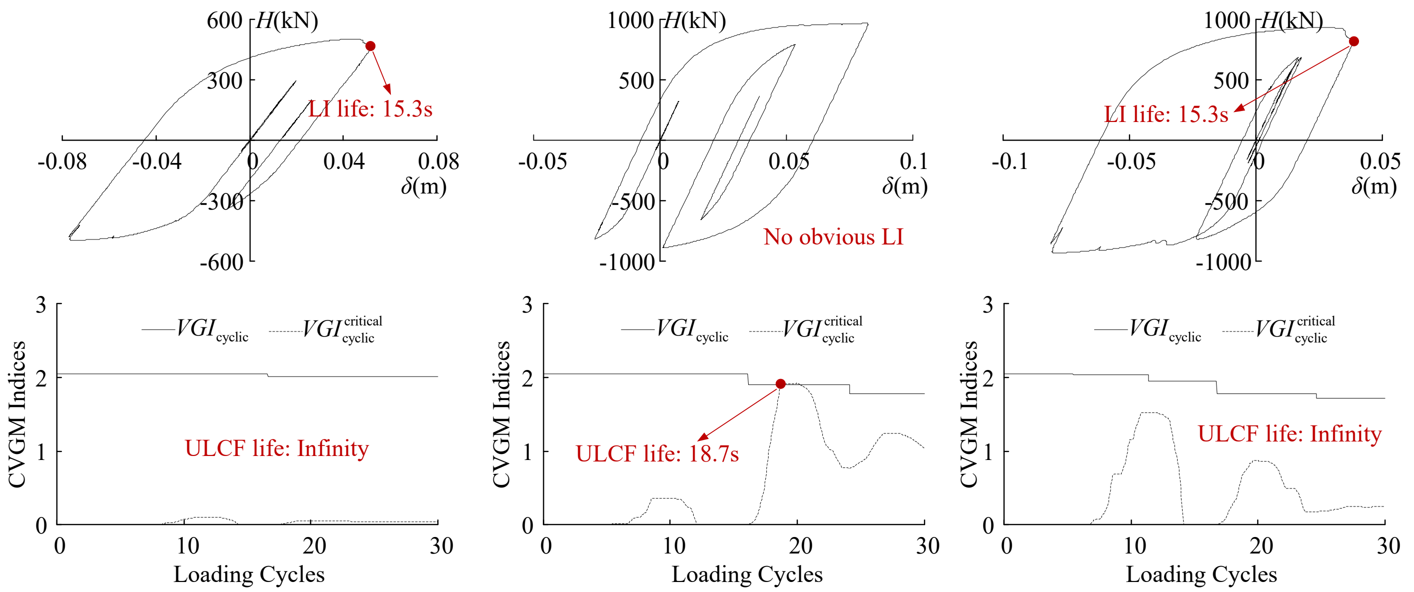

(a) S40-45P20 (b) S30-35P10 (c) S30-35P30

Fig. 14 Seismic performance of piers under Lushan earthquake

6. Conclusions

A simplified seismic design method of steel piers is presented in this study by investigating the failure occurrence priority of LI and ULCF, which are two main potential failure modes of steel piers under severe earthquake. Based on the derived failure occurrence sequence, it is possible to construct piers with the LI failure occurrence priority in the potential seismic area, avoiding the burdensome ULCF check. The main conclusions of this study which could be drawn are as follows:

- The constant amplitude cyclic loading protocol, with the displacement amplitude of each pier's critical displacement δ_{95} and the total loading cycle of 20, can serve as the loading assumption to determine the failure occurrence priority. The qualitative regulation of the failure occurrence priority derived in this paper is the same as that reported in the literature [11].
- The quantitative relationship between the structural parameters and the failure occurrence priority of box section single-column Q345qC steel constructed steel pier, within the structural parameter ranges of $0.25 \leq \lambda_B \leq 0.50$, $0.30 \leq R_R \leq 0.50$, $0.10 \leq P/P_y \leq 0.30$ and $\gamma/\gamma^* = 1.5$, was established.
- Discussions on the seismic performance of steel piers prove that the regulation of the failure occurrence sequence is determined by the mechanical properties of the pier structure, rather than the loading condition.
- Dynamic time-history analyses with real seismic wave inputs were conducted to verify the results of the failure occurrence priority derived by the quasi-static analyses. The damage sequences derived from the two kinds of analyses show good consistency, indicating the reliability of the simplified seismic design method proposed in this study.

Due to the assumed loading protocol applied in this paper, the judgment on the necessity of ULCF checking in this paper is conservative. Piers with the damage priority of ULCF in this study may experience the LI damage before the ULCF under real seismic motion. Although the piers designed using the proposed method are considered to be on the safer side under such a situation, the available structural parameter range is narrowed. In future research, further refinement of the assumed quasi-static loading protocol can be performed to pursue a more accurate relationship between damage priorities and structural parameters according to the seismic motion characteristics of different seismic regions, such as the magnitude, fault parameters and seismic propagation paths.

Acknowledgement

The research in this paper has been conducted as part of the research projects granted by the National Natural Science Foundations of China (51878606 and 52178174). Data for this study are provided by Institute of Engineering Mechanics, China Earthquake Administration. Besides, further appreciation is given to Dassault Systèmes Simulia Corporation for the FE simulation of the powerful commercial FE software ABAQUS-6.14.

References

[1] Kuwamura H., "Transition between fatigue and ductile fracture in steel", Journal of Structural Engineering, 123(7), 864-870, 1997.
[2] Kanvinde A.M., Micromechanical simulation of earthquake-induced fracture in steel structures, Dissertation, Stanford University, 2004.
[3] Nakashima K., Inoue K., and. Tada M., "Classification of damage to steel buildings observed in the 1995 Hyogoken-Nanbu earthquake", Engineering Structures, 20(4), 271-281, 1998.
[4] Subcommittee on Investigation of Seismic Damage of Steel Structure, "Investigation of causes of damage to steel structure on Hanshin-Awaji earthquake disaster", Doboku Gakkai Ronbunshu, 64, 17-30, 2000. (In Japanese)
[5] Miller D.K., "Lessons learned from the Northridge earthquake", Engineering Structures, 20(4), 249-260, 1998.
[6] Ge H.B. and Kang L., "Ductile crack initiation and propagation in steel bridge piers subjected to random cyclic loading", Engineering Structures, 59, 809-820, 2006.
[7] Goto Y., Jiang K.S. and Obata M., "Stability and ductility of thin-walled circular steel columns under cyclic bidirectional loading". Journal of Structural Engineering. 132(10), 1621-1631, 2006.
[8] Goto Y., Ebisawa T., Lu X.L., Lu W.S., "Ultimate state of thin-walled circular steel columns subjected to biaxial horizontal forces and biaxial bending moments caused by bidirectional seismic accelerations", Journal of Structural Engineering, 141(4), 04014122, 2015.
[9] Zhuge H.Q., Xie X. and Tang Z.Z., "Lengths of damaged zones of steel piers under bidirectional horizontal earthquake components", China Journal of Highway and Transport, 32(8), 79-91, 2019. (In Chinese)
[10] Li S.L, Lin J.H., Zhuge H.Q., Xie X. and Cheng C., "Ultra-low cycle fatigue fracture initiation life evaluation of thick-walled steel bridge piers with microscopic damage index under bidirectional cyclic loading", Structures, 43, 669-681, 2022.
[11] Ge H.B., Kang L. and Tsumura Y., "Extremely low-cycle fatigue tests of thick-walled steel bridge piers", Journal of Bridge Engineering, 18(9), 858-870, 2013.
[12] Jenothan M., Jayasinghe J. A. S. C. and Bandara C. S., "Lateral behaviour and performance evaluation of steel piers under cyclic lateral loading", Journal of Constructional Steel Research, 201, 107764, 2023.
[13] Ge H.B. and Usami T., "Cyclic tests of concrete-filled steel box columns", Journal of Structural Engineering, 122(10), 1169-1177, 1996.
[14] Goto Y., Muraki M. and Ebisawa T., "Ultimate state and design of thin-walled circular steel columns under bi-directional seismic excitations", Kozo Kogaku Ronbunshu, 629-642, 2009.
[15] Gao S.B., Usami T. and Ge H.B., "Ductility evaluation of steel bridge piers with pipe sections. Journal of Engineering Mechanics", 124(3), 260-267, 1998.
[16] Specifications for Highway Bridges, Part II: Steel Bridges 2017., Japanese Road Association, Tokyo, Japan, 2017.
[17] Guide Specifications for LRFD Seismic Bridge Design 2011., American Association of State Highway and Transportation Officials, Washington, America, 2017.
[18] Specifications for Design of Highway Steel Bridge 2017., Ministry of Transport of the People's Republic of China, Beijing, China, 2017.
[19] Coffin L.F., "A study of the effects of cyclic thermal stresses on a ductile metal", Trans. ASME, 76, 931-50, 1954.
[20] Manson S.S., "Fatigue: a complex subject – some simple approximations", Experimental Mechanics, 5, 193-226, 1965.
[21] Tateishi K., Hanji T. and Minami K., "A prediction model for extremely low cycle fatigue strength of structural steel", International Journal of Fatigue, 29(5), 887-896, 2007.
[22] Xue L., "A unified expression for low cycle fatigue and extremely low cycle fatigue and its implication for monotonic loading", International Journal of Fatigue, 30(10), 1691-1698, 2008.
[23] Xie X., Cheng C. and Li S. L., "A deformation history-based approach for ultra-low cycle fatigue damage evaluation of steel structures", International Journal of Steel Structures, 20(4), 1378-1392, 2020.
[24] Tamura H., Sasaki E., Yamada H. and Katsuchi H., "Analytical study focusing on stress triaxiality on factor of brittle fracture during earthqakes in steel bridge bents", Structural Engineering & Earthquake Engineering, 66(3), 420-434, 2010. (In Japanese)
[25] Tamura H. and Sasaki E., "A study on modified weibull stress based evaluation of brittle fracture occurrence during earthquakes in steel members", Structural Engineering & Earthquake Engineering, 71(2), 173-185, 2015. (In Japanese)
[26] Liu Y., Kang L. and Ge H.B., "Experimental and numerical study on ductile fracture of structural steels under different stress states", Journal of Constructional Steel Research, 158, 381-404, 2019.
[27] Tong L.W., Huang X.W., Zhou F. and Chen Y.Y., "Experimental and numerical investigations on extremely-low-cycle fatigue fracture behavior of steel welded joints", Journal of Constructional Steel Research, 119(1), 98-112, 2016.
[28] Kanvinde A. M., Deierlein G. G., Kanvinde A. M. and Deierlein G. G., "Cyclic void growth model to assess ductile fracture initiation in structural steels due to ultra low cycle fatigue", Journal of Engineering Mechanics, 133(6), 701-712, 2007.
[29] Liao F.F., Micromechanical simulation of earthquake-induced fracture in steel structures, Dissertation, Tongji University, 2012. (In Chinese)
[30] Liao Y.H., Research on ultra low cycle fatigue properties and fracture mechanism of steel bridge welded joint, Dissertation, Zhejiang University, 2018. (In Chinese)
[31] Usami T., Gao S.B. and Ge H.B., "Elastoplastic analysis of steel members and frames subjected to cyclic loading", Engineering Structures, 22(2), 135-145, 2000.
[32] Liu N.F., Gao S.B., "Ductility prediction of stiffened steel pipe-section bridge piers", Journal of Harbin Institute of Technology, 49(3), 138-143, 2017. (In Chinese)
[33] Xie X., Zhuge H.Q., Tang Z.Z., Wang T. and Liao Y-H., "Damage characteristics of thin-walled steel arch bridges subjected to in-plane earthquake action", Journal of Constructional Steel Research, 151, 70-82, 2018.
[34] Tsai C.Y., Tsai K.C., Li C.H., Wu C.C., Lin K.C. and Jhuang S.J., "Seismic fracture evaluation of diaphragm joints in welded beam-to-box column moment connections", Earthquake Engineering & Structural Dynamics, 49(13), 1344-1362, 2020.
[35] Wang Y.M., Zhang H.D., Ju J.S. and Fu Y.D., "Influence of welding residual stress on ultra-low cycle fatigue properties of beam-column joints in steel frame", Strength of Materials, 54(4), 734-746, 2022.
[36] Noferesti H., Razmkhah M.H. and Gerami M., "Laboratory and ultra-low cycle fatigue evaluation of the seismic performance of BFP connection with different amounts of pre-tension in bolts", Journal of Constructional Steel Research, 212, 108295, 2023.
[37] Zhang Y.L., Wang W., Huo H.W., Wang Y. and Fang C., "Cyclic void growth model to assess ductile fracture initiation in structural steels due to ultra low cycle fatigue", Journal of Constructional Steel Research, 215, 108561, 2024.
[38] Ge H.B., Gao S.B. and Usami T., "Stiffened steel box columns. Part 1: Cyclic behaviour", Earthquake Engineering & Structural Dynamics, 29(11), 1691-1706, 2000.
[39] Shi Y.P. and Zhou Y.R., Detailed explanation of ABAQUS finite element analysis examples, Mechanical Industry Press, Beijing, 2006.
[40] Zhuge H.Q., Xie X., Li S-L., Wang J.D., "Seismic performance test and practical calculation method of thin-walled square-section steel piers under horizontal bi-directional seismic excitations", China Civil Engineering Journal, 53(12), 74-85, 2020. (In Chinese)
[41] Tang Z.Z., Xie X., Wang T. and Wang J.Z., "Study on FE models in elasto-plastic seismic performance evaluation of steel arch bridge", Journal of Constructional Steel Research, 113, 209-220, 2015.
[42] Chen S.X., Xie X., Zhuge H.Q., "Hysteretic model for steel piers considering the local buckling of steel plates", Engineering Structures, 183, 303-318, 2019.
[43] Pallant J., SPSS survival manual: a step by step guide to data analysis using SPSS for windows version 15, Open University Press, London, 2007.